Materials Science & Engineering A 948 (2025) 149278

Contents lists available at ScienceDirect

Materials Science & Engineering A

journal homepage: www.elsevier.com/locate/msea

Deformation, strength and corrosion resistance evolutions of AA7475 under creep-ageing with various pre-treatments

Xi Wang [a], Zhusheng Shi [b,c,*], Jianguo Lin [d]

[a] Department of Mechanical Engineering, University of Science and Technology Beijing, Beijing, China
[b] Foshan Xianhu Laboratory, Foshan, 528200, China
[c] Department of Mechanical Engineering, Imperial College London, London, SW7 2AZ, UK
[d] Department of Industrial and Systems Engineering, The Hong Kong Polytechnic University, Hong Kong, China

ARTICLE INFO

Keywords:
Creep-ageing
AA7475
Creep deformation
Strength evolution
Corrosion resistance
Microstructural evolution

ABSTRACT

Multi-step ageing has been developed as a novel treatment for 7xxx aluminium alloys to achieve both high strength and superior corrosion resistance. When creep-ageing these multi-step aged Al-Zn-Mg-Cu alloys to fabricate large scale aerospace components, however, effective strategies to enhance their creep deformation while maintaining a satisfactory balance between strength and corrosion resistance remain lacking. This study systemically investigated the evolution of deformation, strength and corrosion resistance during creep-ageing of a multi-aged AA7475 with various pre-treatments including stress-free and stressed pre-ageing. The effects of the pre-treatments on the material behaviour were examined through uniaxial creep-ageing and subsequent tensile tests, intergranular corrosion (IGC) tests, and corresponding microstructural investigations. It was found that during the creep-ageing process, the creep deformation was promoted, while the strength and corrosion resistance were reduced in the pre-treated specimens when compared to the as-received material. Specifically, the tensile creep aged (TCA) pre-treated specimens exhibited the largest reduction in material strength, while those with pre-aged initial state have the most decrease in corrosion resistance. Creep-ageing of materials in various initial states led to the increase in grain boundary precipitate (GBP) size and precipitate free zone (PFZ) width to varying extents, as well as diverse distributions of precipitates along grain boundaries, which exerted substantial effects on the deformation, strength evolution, and corrosion resistance of the material. This study provides valuable insights into developing feasible treatment strategies to improve creep deformation and enhance creep-ageing efficiency in high strength Al-Zn-Mg-Cu alloys, while maintaining an optimal balance between strength and corrosion resistance of the material.

1. Introduction

Al-Zn-Mg-Cu alloys, also known as 7xxx aluminium alloys, have been widely adopted as structural materials in the aerospace industry due to their high strength and low density [1,2]. When the aluminium alloys in this series are subjected to ageing treatment, the precipitation sequence typically follows the transformation from a supersaturated solid solution (SSS) state to Guinier-Preston (GP) zones, following to η', and finally to η, where the GP zones and metastable η' precipitates contribute most to the strengthening of the material [3,4]. By utilising precipitation hardening through artificial ageing, the Al-Zn-Mg-Cu alloys can achieve their peak strength as the T6 temper with appropriate time and temperature. However, the material's corrosion resistance is traded off for strength when achieving T6 temper, which restricts its practical use [4,5]. As a result, various ageing treatments have been developed to tailor 7xxx aluminium alloys to achieve the desired synergy of strength, toughness, and corrosion resistance [6,7].

Multi-step ageing, as a novel artificial ageing treatment method, has been found effective for 7xxx aluminium alloys in achieving high strength while maintain satisfactory corrosion resistance [5]. By applying solution heat treatment (SHT), followed with two-step ageing at 120 °C for 6 h and 160 °C for 16 h to achieve the T74 temper, the Al–6.0Zn–2.3Mg–1.8Cu (wt.%) alloy achieved a balanced synergy between strength and corrosion resistance [8]. Additionally, by employing a three-step ageing process including pre-ageing, retrogression, and subsequent re-ageing, the retrogression and re-ageing (RRA) treatment

* Corresponding author. Department of Mechanical Engineering, Imperial College London, London SW7 2AZ, UK.
E-mail address: zhusheng.shi@imperial.ac.uk (Z. Shi).

https://doi.org/10.1016/j.msea.2025.149278
Received 27 April 2025; Received in revised form 1 October 2025; Accepted 13 October 2025
Available online 14 October 2025

provides an alternative approach for the 7xxx aluminium alloys to achieve high strength comparable to their T6 temper while providing significantly improved corrosion resistance [7,9]. Extensive investigations have demonstrated the ageing temperatures and durations used in multi-step ageing can exert substantial effects on the mechanical properties of Al-Zn-Mg-Cu alloy, and prominent results have been achieved by adopting proper ageing treatments to control the precipitation processes and distribution in these alloys, thereby to favour the enhancement of strength and corrosion resistance [10,11].

When employing 7xxx aluminium alloys to fabricate large-scale and thin-walled components such as wing skins and fuselage panels, creep age forming (CAF) has emerged as a breakthrough technique over the past two decades [12,13]. This fabrication method combines metal forming and age hardening by inducing creep deformation in the material under controlled temperature and displacement. The effectiveness of CAF has been adequately demonstrated in fabricating components for both civil and military aircraft [12]. However, with the continuous enhancement of material strength driven by advancements in aluminium alloy manufacturing and ageing treatment techniques, challenges have emerged in forming these advanced alloys through CAF [14,15]. When using two-step aged aluminium alloy 7050 (AA7050) to fabricate single curved strips with a radius ranging from 1500 to 2500 mm, springback in CAF can reach as high as 77 %–85 % [16]. Similarly, a maximum of 76 % springback can occur when fabricating stiffened panels using AA7B04 with multi-step ageing treated to T651 temper through CAF [17]. The high springback in CAF can significantly affect forming accuracy, especially for components with more complex contours. Therefore, it is crucial to find ways to enhance creep deformation of these advanced Al-Zn-Mg-Cu alloys during CAF while maintaining their mechanical properties at an optimal level.

Extensive studies on enhancing creep deformation for high strength aluminium alloys during CAF have been conducted in recent years, among which pre-deformation and plastic loading become the measures attracting the most attention [18,19]. By introducing mobile dislocation through pre-deformation to reduce the threshold stress during subsequent creep-ageing, AA2219 demonstrated a 2 times increase in creep deformation when pre-stretched to 7 % prior to creep-ageing at 165 °C and 150 MPa [20]. AA7050 demonstrated a continuous increase in creep deformation during the uniaxial stress relaxation tests as the applied stress shifted from the elastic to the plastic loading region [21]. Additionally, increasing attention has been focused on combining multi-step ageing treatment with the creep-ageing process for Al-Zn-Mg-Cu alloys to enhance the CAF efficiency. A novel multi-step creep-ageing method was employed on AA7050 to increase deformation in creep-ageing, in which the alloy had undergone SHT, pre-stretching, and was creep-aged at 120 °C for 6 h and 177 °C for 7 h under specific stresses [21]. A two-step creep-ageing process, including creep-ageing under 300 MPa at 180 °C for 2–3 h following with 120 °C for 4 h, was employed to AA7B50 in T6 temper [22]. This process resulted a noticeable creep deformation enhancement compared to the one-step creep-ageing at 140 °C under 300 MPa [22]. However, a noticeable decrease in material strength was identified during creep-aging of AA7050 in plastic region, as well as in AA7B50 undergone two-step creep-ageing [22,23]. This decrease can be attributed to the accelerated coarsening of precipitates under higher stress [23].

In addition, it was observed that the corrosion resistance of Al-Zn-Mg-Cu alloy is highly sensitive to creep-ageing conditions, and varying stress and ageing time can exert considerable effects [24,25]. The corrosion resistance of T6 temper AA7075 was found to initially enhanced with the elongation of pre-ageing time from 20 to 40 min at 185 °C, while decreased when the pre-ageing time was further increased from 40 to 60 min at the same temperature [25]. Therefore, challenges still exist in achieving satisfactory balance among creep deformation enhancement, material strength, and corrosion resistance for Al-Zn-Mg-Cu alloys, especially for alloys that have undergone multi-step ageing treatment to optimise their mechanical state for service.

This study focuses on addressing the gaps in understanding the material behaviours of AA7475 under creep-ageing with various pre-treatments and aims to investigate measures that improve creep deformation behaviour while optimising their mechanical and corrosion properties. By employing various pre-treatments including stress-free and stressed pre-ageing on the multi-step aged AA7475 in the specific temper for age forming (TAF), along with microstructural investigations and intergranular corrosion (IGC) tests, the creep deformation behaviour, strength evolution, and corrosion resistance of multi-aged AA7475 in creep-ageing across various pre-treatments were systemically investigated. The variations in microstructural evolution induced by different pre-treatments during creep-ageing, including size changes in precipitates and at the scale of grain boundaries, were illustrated along with the correlations between these microstructural variations and the observed different material behaviours. Thus, this study provides insights into establishing feasible treatment measures to enhance creep-ageing efficiency in high strength Al-Zn-Mg-Cu alloys, while maintaining a balanced synergy of strength and corrosion resistance.

2. Material and experimental procedures

The material used in this study was a 100 mm thick 7475 aluminium alloy plate, with its composition provided by the material supplier demonstrated as in Table 1. The as-received material had undergone SHT, followed by 2 %–3 % pre-deformation, and a multi-step ageing treatment. The ageing was performed between 100 °C and 120 °C for 7 h, and then at 160 °C–175 °C for 1 h respectively. This specially developed treatment was designed to produce a material condition referred to as TAF (Temper for Age Forming) and achieve the properties comparable to T74 while reducing nearly 50 % process time [26].

The specimens used in this study were cut along the rolling direction of the plate at the depth of 25 mm below the plate surface. The geometry and dimensions of the specimen are shown in Fig. 1a. Uniaxial creep-ageing and tensile tests were conducted using this type of specimen. For subsequent electron backscatter diffraction (EBSD), transmission electron microscopy (TEM), and intergranular corrosion (IGC) tests, the middle part of the specimen was cut and used, as shown in Fig. 1b.

Uniaxial tensile creep-ageing (CA) tests were conducted using an Instron 5584 load frame equipped with an elevated temperature chamber. Before creep-ageing, pre-treatments were carried out and the creep-ageing tests were conducted under four different initial states, including the as-received, pre-aged (PA), tensile creep aged (TCA), and compressive creep aged (CCA) states. As shown in Fig. 2, for the as-received state, the specimen directly underwent creep-ageing without any pre-treatment. For PA, TCA and CCA, the specimens respectively underwent pre-treatment at 174 °C for 1 h at different stress states: no stress was applied in the PA state, while tensile and compressive stresses of 120 MPa were respectively applied in TCA and CCA. Regarding the creep-ageing stage, as exhibited in Fig. 2, the same conditions were applied to all four initial states, with each specimen creep aged under 135 MPa at 174 °C for 6 h. The temperature was monitored using thermocouples attached to the centre of the specimen. The same loading rate of 0.5 kN/min was applied for all creep-ageing tests. Uniaxial tensile tests were conducted before and after creep-ageing for the initial states of as-received, PA, TCA, and CCA, using a strain rate of 1×10^{-4} s^{-1}. Table 2 lists the experimental scheme for creep-ageing and tensile tests under various conditions.

Microstructural investigations of the material in different initial

Table 1
Chemical composition of the investigated 7475 aluminium alloy.

Element	Zn	Mg	Cu	Cr	Fe
wt%	5.2–6.2	1.9–2.6	1.2–1.9	0.18–0.25	Min-0.12
Element	**Si**	**Mn**	**Ti**	**Al**	
wt%	Min-0.1	Min-0.06	Min-0.06	Remainder	

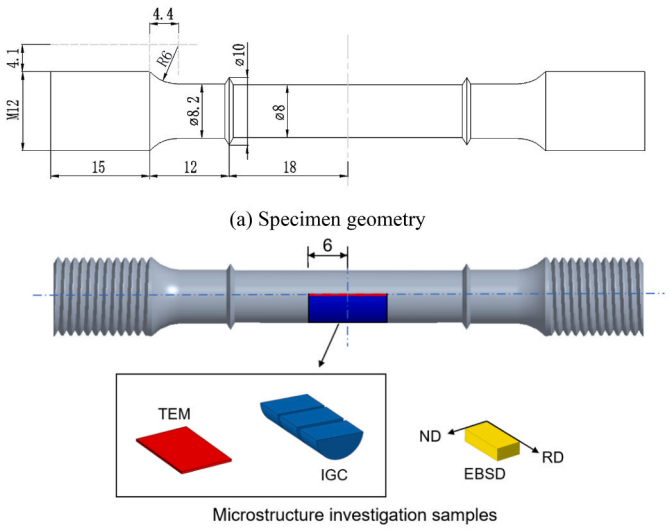

Fig. 1. Specimen geometry adopted in this study (dimension in mm).

states before and after creep-ageing were conducted using transmission electron microscopy (TEM) and electron backscatter diffraction (EBSD). TEM specimens were obtained from a 12 mm × 8 mm TEM sample with a thickness of 0.5 mm, which was cut from the symmetric plane as shown in Fig. 1b. The sample was mechanically ground to a foil with thickness less than 80 μm and then punched into 3 mm discs for electropolishing. Electropolishing was conducted using a mixture with a volume ratio of 1:3 of nitric acid to methanol, at the voltage of 20 V and within a temperature range of −30 °C to −20 °C. The EBSD specimen with dimensions of 8 mm × 4 mm x 2 mm, as shown in Fig. 1b, was cut along the plane parallel to the rolling direction and the normal direction from the AA7475 plate at the same depth as the uniaxial specimen. For EBSD observation, the specimen had undergone mechanical grinding and electropolishing in a mix solution of 10 vol% perchloric acid and 90 vol% ethanol at a voltage of 15 V and temperature of −30 °C to −25 °C for 5 s. The specimen was scanned using a ZEISS Sigma 360 field emission scanning electron microscope with a step length of 1.68 μ m. The test scheme for microstructure investigations including TEM and EBSD is illustrated in Table 3.

For each treatment condition, the IGC sample was evenly cut into three specimens along its length direction as shown in Fig. 1b. During the test, the specimen was immersed in a mixture solution of 1.0 Mol/L NaCl, 0.5 Mol/L HNO_3, and 0.01 Mol/L H_2O_2, and maintained at 30 °C in a water bath for 24 h. Before placing each specimen in the IGC solution, its weight and dimensions were measured. At the end of the test, the specimen was subjected to ultrasonic cleaning for 30 s, air-dried for 2 h, and then weighed again. Weight loss analysis was performed using the experimental data to quantitively evaluate the corrosion resistance of each specimen. The test scheme for IGC test across various treatment conditions is also listed in Table 3.

3. Experimental results

The creep deformation of AA7475 in various initial states, including the as-received, PA, TCA, and CCA, is shown in Fig. 3, which demonstrates the complete creep deformation profiles, including both the pre-

Table 2
Test scheme for creep-ageing and tensile tests under various treatment conditions.

Treatment condition	Test scheme
As-received	Tensile test
As-received & CA	6 h CA, then tensile test
PA	PA, then tensile test
PA & CA	PA + 6 h CA, then tensile test
TCA	TCA, then tensile test
TCA & CA	TCA +6 h CA, then tensile test
CCA	CCA, then tensile test
CCA & CA	CCA +6 h CA, then tensile test

Table 3
Test scheme for TEM, EBSD, and IGC under various treatment conditions.

Treatment condition	Test scheme
As-received	TEM, EBSD, and IGC
As-received & CA	TEM and IGC
PA	TEM
PA & CA	TEM and IGC
TCA	TEM
TCA & CA	TEM and IGC
CCA	TEM
CCA & CA	TEM and IGC

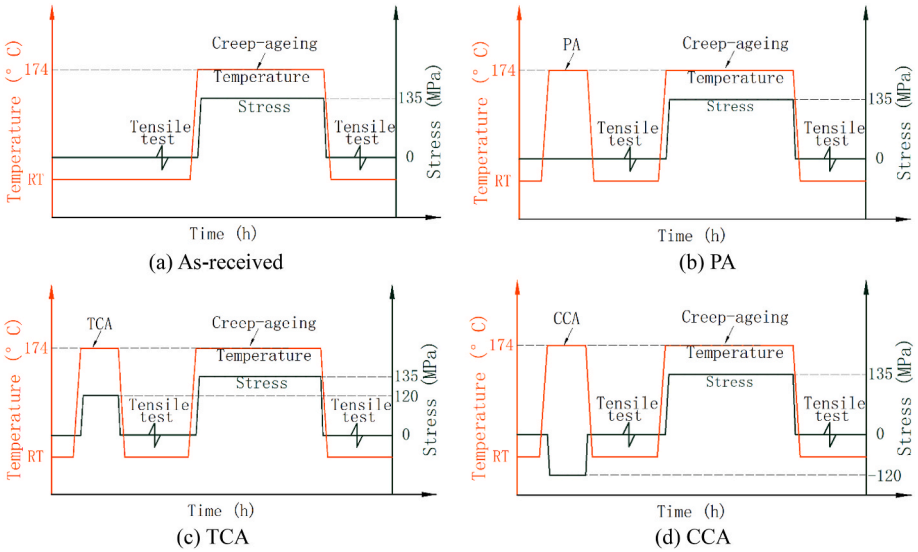

Fig. 2. Schematic of thermal and loading profiles for creep-ageing at the conditions of as-received, PA, TCA, and CCA. RT stands for room temperature.

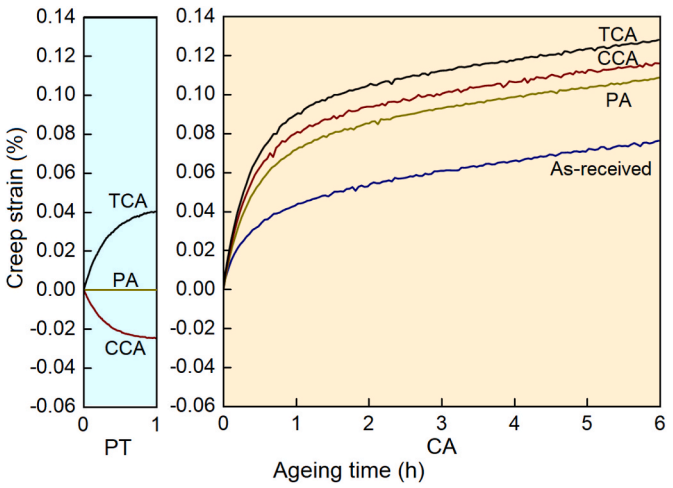

Fig. 3. Creep deformation curves at 174 °C and 135 MPa, including both the pre-treatment (PT) and creep-ageing (CA) stages.

treatment (PT) and creep-ageing (CA) stages. During the pre-treatment stage, the PA treatment was carried out at 174 °C for 1 h without applied stress. In contrast, the TCA and CCA pre-treatments were respectively preformed under tensile and compress stress of 120 MPa at 174 °C for 1 h. All the specimens were subsequently creep aged at 174 °C under the stress of 135 MPa for 6 h. As can be observed in Fig. 3, during the pre-treatment stage, the creep deformation of TCA reached 0.04 % after 1 h under the tensile stress of 120 MPa, while CCA accumulated a strain of 0.025 % under the same stress applied in the compressive direction. The curves in the CA stage from 0 to 6 h in Fig. 3 illustrate the creep deformation behaviour of the material in the subsequent creep-ageing stage with various initial states. It should be noted that the creep deformation results were obtained under the same creep-ageing condition of 135 MPa and 174 °C. During the creep-ageing stage, the deformation with the initial state TCA exhibits the largest deformation, with a creep strain around 0.13 % after creep-aged of 6 h. In contrast, the as-received state, which is multi-aged to TAF temper, has the lowest creep strain of 0.08 % after 6 h. The deformation for initial states of PA and CCA are both lower than that of TCA, with the PA state showing the lowest creep strain.

Fig. 4 quantitively illustrates the effects of different pre-treatments on the creep deformation of AA7475, presenting the creep deformation rate and deformation ratio at various intervals of the creep-ageing process. As observed in Fig. 4a, the creep deformation rate during the initial period of creep-ageing from 0 to 2 h shows significant variance, with the rate of TCA 1.94 times higher than the rate of the as-received. In contrast, the rate during the latter period of creep-ageing from 2 to 6 h demonstrate minor differences across various initial states, with a maximum difference of 7 % between the as-received and PA states. In addition, as shown in Fig. 4b, the creep deformation ratio is calculated by respectively comparing the creep strain of PA, TCA, and CCA to the strain of the as-received state over different periods during creep-ageing, including the total strain accumulated after 6 h of creep-ageing, as well as during the intervals of 0–2 h, and 2–6 h. The creep deformation ratios of 0–6 h for PA, CCA, and TCA are all larger than 1. When comparing the ratios for the periods of 0–2 h and 2–6 h, the ratio of the former is significantly larger than the latter, indicating that the promotion of creep deformation for PA, CCA, and TCA primarily occurred during the initial creep-ageing period between 0 and 2 h. The significant differences in creep deformation rates during the initial period, as well as the varying creep deformation promotion effects compared to the as-received are certainly related to the initial states of PA, CCA, and TCA treatments and their corresponding influences on subsequent creep deformation behaviour will be discussed later.

The strength evolution before and after creep-ageing across various initial states is presented in Fig. 5. Overall, the behaviour is similar for the different initial states both before and after creep-ageing. Fig. 5a demonstrates the uniaxial tensile stress-strain curves for specimens with and without pre-treatments, i.e. the as-received, PA, TCA and CCA, before creep-ageing. The as-received material exhibits the highest yield strength, while the pretreated specimens demonstrate reduced yield strength compared to the as-received state (about 1 % lower) while very similar to each other (about 2 MPa difference). Fig. 5b shows the stress-strain curves of the specimens after creep-ageing for 6 h across various pre-treatments, among which the specimen with the initial state of as-received again exhibits the highest strength, while the specimen with the TCA initial state shows the lowest strength. In addition, it can be observed that the strength of the material decreased after creep-ageing with all initial states compared to their strength before creep-ageing. To further confirm the reliability of the observed trend, repeated tests were performed with the results provided in Appendix A.

Fig. 6 further quantitatively illustrates the strength evolution before and after creep-ageing across various pre-treatments. Fig. 6a reflects the values of the specimen across various treatments. Fig. 6b demonstrates the strength reduction percentage calculated using the equation $(S_0 - S_x)/S_0$, where S_0 and S_x denote the yield strength of the as-received material and yield strength of the material across various pre-treatments before and after creep-ageing. As shown in Fig. 6, the strength reduction of specimens subjected to PA, TCA, and CCA pre-treatments compared to the as-received material is similar, with the reduction percentage ranging from 1.2 % to 1.6 %. On the other hand,

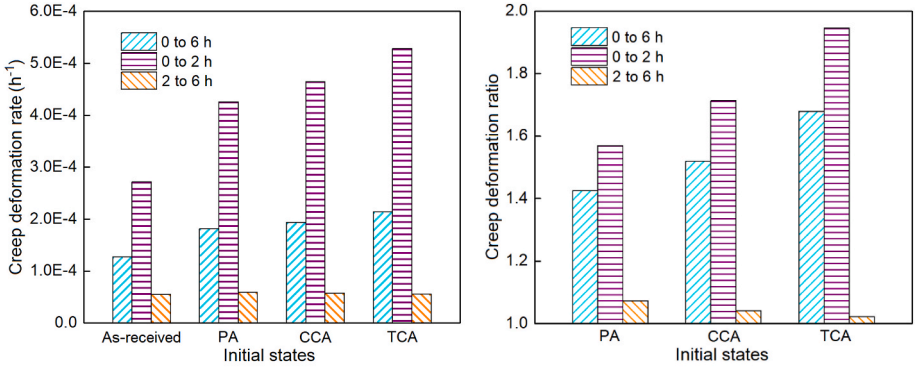

(a) Creep deformation rate (b) Creep deformation ratio

Fig. 4. Creep deformation rate and deformation ratio across different periods of creep-ageing including 0–6 h, 0–2 h, and 2–6 h. The notation "A to B h" in (a) and (b) indicates the specific time intervals of A h to B h during creep-ageing. The creep deformation ratio indicates the deformation of PA, CCA, and TCA relative to the deformation of the as-received during corresponding periods.

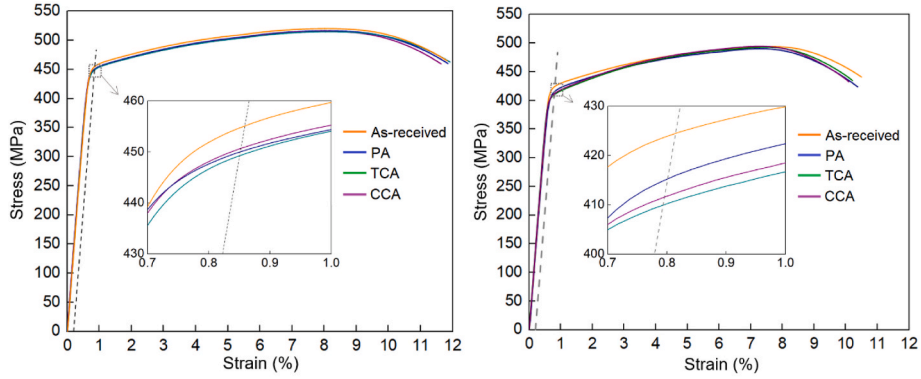

(a) Stress-strain curves before creep-ageing (b) Stress-strain curves after creep-ageing

Fig. 5. Stress-strain curves with initial states of the as-received, PA, TCA, and CCA shown in (a), and after creep-ageing at 135 MPa and 174 °C after 6 h shown in (b).

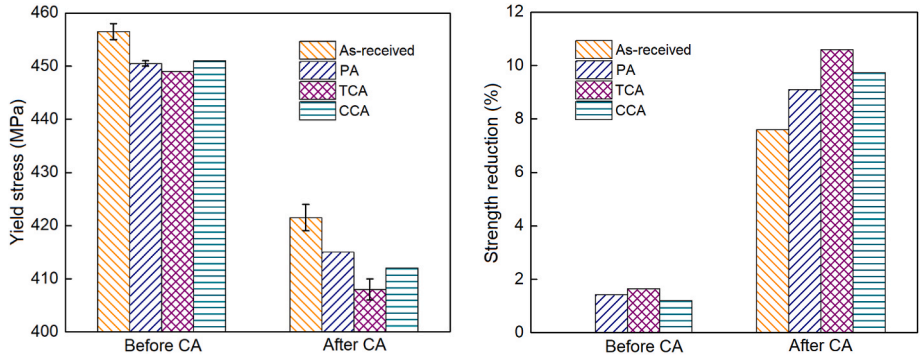

(a) Yield strength before and after CA (b) Strength reduction before and after CA

Fig. 6. Yield strength and strength reduction percentage (relative to the as-received) across various pre-treatments, both before and after creep-ageing. "CA" in (a) and (b) denotes creep-ageing at 174 °C for 6 h.

after creep-ageing for 6 h, the yield strength of specimens in all conditions decreases more significantly compared to the strength reduction observed in specimens across various pre-treatments before creep-ageing, with the largest reduction in TCA (10.6 %) and the smallest reduction in the as-received (7.6 %).

The precipitate size in the as-received state, as well as its evolution after various pre-treatments and undergone subsequent creep-ageing was investigated using TEM to understand the microstructural evolution. Fig. 7 shows the selected bright field TEM images of the material at different treatment states. The specimens of the as-received condition, after CCA pre-treatment, and creep-aged for 6 h with or without TCA/CCA treatment, exhibiting noteworthy differences in precipitate morphologies, are selected for comparison in Fig. 7. As shown in the figure, two different precipitates morphologies with round and needle-like shapes are observed, which respectively correspond to the two major strengthening precipitates in the Al-Cu-Mg alloys, i.e. GP zones and η' precipitates [27,28]. To further confirm the presence of spherical GP zones and needle-like η' precipitates, the selected area diffraction (SAED) pattern along $[112]_{Al}$ zone axis was studied, and energy dispersive X-ray spectroscopy (EDS) analysis was conducted on the GP zone and η' precipitate as demonstrated in Fig. 7b. In Fig. 7b, the diffraction spots observed near 2/3{220} positions in the SAED pattern along $[112]_{Al}$ zone axis indicates the presence of semi-coherent η' precipitates [29]. In addition, the EDS analysis results for GP zone and η' precipitate demonstrate a dominance of Al, Zn, Mg, and Cu elements, which further verified the identifications of these two precipitates [30,31].

Fig. 8 shows the statistical results for the size of the GP zone and η' precipitate as well as their quantity ratios in the materials of the as-received, undergone various pre-treatments, and subjected to following subsequent 6 h creep-ageing. The statistical results for each treatment state are obtained from more than 100 precipitates with corresponding TEM images taken from different locations. As can be observed in Fig. 8a, when comparing the average size of η' precipitate to GP zone across the as-received state, pre-treated states (PA, TCA, CCA), and subsequent creep-aged states, η' precipitate is all larger than the GP zone. Additionally, little variation in the average size of the GP zone is identified among different states. Fig. 8b demonstrates the precipitate size increase before and after 6 h of creep-ageing for the non-pre-treated state and the pre-treated states. The size increase of η' precipitate during 6 h creep-ageing is significantly greater than the size increase of the GP zone across all states, with the highest increase of 13.1 nm for η' precipitate and 1.2 nm for the GP zone, both observed in the TCA states. Fig. 8c illustrates the relative frequency of η' precipitate and GP zone across various states. It can be observed that the ratio of η' precipitate increased after creep-ageing, with the pre-treated and creep aged states exhibiting higher ratios than the directly creep aged.

Fig. 9 shows the bright field TEM images of grain boundaries from specimens in various conditions as well as the statistic results of grain boundary precipitates (GBPs) size and precipitate free zones (PFZs) width. Along the grain boundaries in these specimens as shown in Fig. 9, both GBPs and PFZs are observed with different morphologies in the various states. In Fig. 9a, the GBPs in the as-received state are randomly distributed along the grain boundary, with larger sizes compared to the precipitates in the surrounding alloy matrix. Additionally, PFZs are observed along the grain boundary. After creep-ageing for 6 h, larger GPBs and clearer PFZs are formed compared to the as-received state. as shown in Fig. 9b. In the specimen initially PA and followed with 6 h

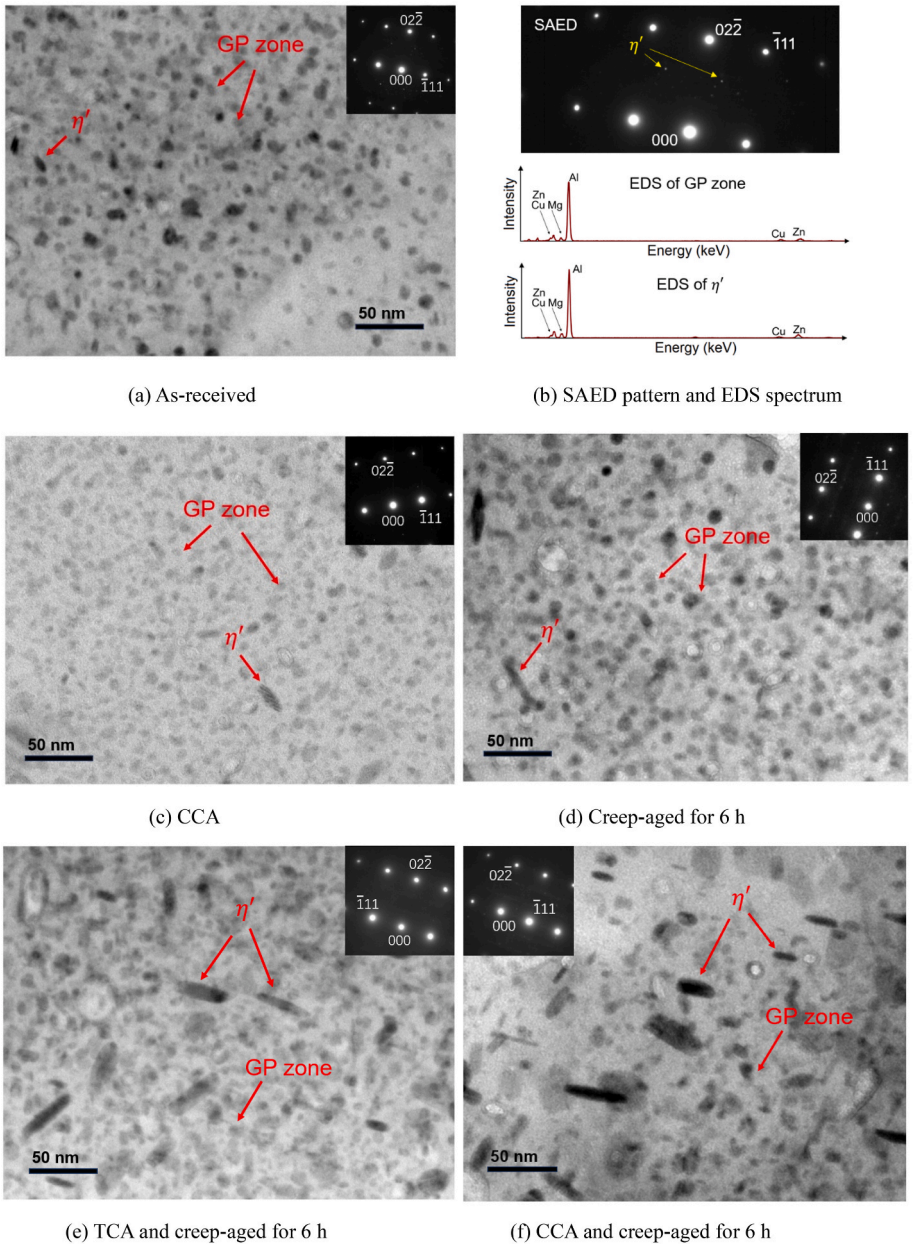

Fig. 7. Bright field TEM images and selected area diffraction (SAED) patterns along $[112]_{Al}$ zone axis. The enlarged SAED pattern and energy dispersive X-ray spectroscopy (EDS) spectrums for GP zone and η' precipitates are exhibited in (b).

creep-ageing as exhibited in Fig. 9c, more distinctly increased GPBs and wider PFZs are observed. For the TEM images of grain boundaries that have undergone TCA/PCA pre-treatment and subsequently creep aged for 6 h as shown in Fig. 9d and e, the numbers of GBPs for both pre-treatments are increased compared to the as-received state (Fig. 9a). On the other hand, the GBP size and PFZ width for TCA and PCA (Fig. 9d and e) are reduced compared to those of the as-received along the grain boundary. Fig. 9f illustrates the statistical results of GBP size and PFZ width across various states. For each state, more than 20 GBPs and 15 locations of PFZ width were measured along different grain boundaries. The results demonstrate an increase trend in GBPs and PFZs after creep-ageing compared to the as-received condition, with the PA and CA specimen exhibiting the largest precipitate size and PFZ width respectively.

EBSD analysis is conducted to investigate the material in its as-received state to further understand the microstructural characteristics at the grain boundary areas. It should be noted that in the circumstances of creep-ageing under small strain (less than 0.2 %) and low ageing temperature (less than 1/3 of the material's melting point), grain recrystallisation is barely induced leading to very subtle evolutions regarding the grain size and the misorientation angle, which cannot be accurately captured by EBSD [32,33]. Therefore, only the material in the as-received state is selected for investigation. The obtained inverse pole figure (IPF), geometry necessary dislocation (GND) density maps, and statistical distributions of kernel average misorientation (KAM) angles as well as GND densities are shown in Fig. 10. From the IPF map shown in Fig. 10a, it can be observed that the grains in the TAF temper 7475 aluminium alloy are significantly elongated along the rolling direction. The statistical results of KAM angles presented in Fig. 10b illustrate the dominance of low-angle grain boundary (LAGB) and GND in the material, with the angles mostly distributed below 3°. The GND density map shown in Fig. 10c indicates that GNDs are primarily accumulated surrounding the grain boundaries. Fig. 10d shows the statistical distribution of GND densities, which predominantly fall within the range from

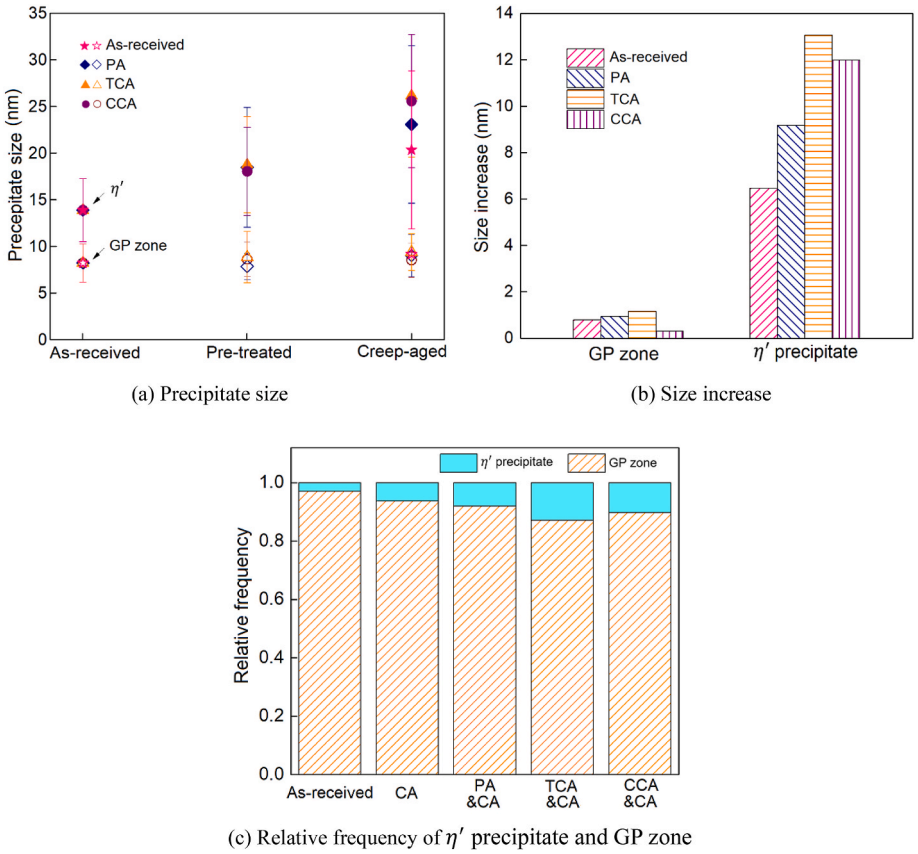

(a) Precipitate size (b) Size increase

(c) Relative frequency of η' precipitate and GP zone

Fig. 8. Statistical results of average precipitate size evolution and size increase, as well their number ratios. The size increase in (b) demonstrates the difference between the precipitate size after creep-ageing and the as-received.

0 to 1.5 × 10^{14}/m^2. The statistical results of KAM and GND density demonstrate that the grain boundaries are predominantly LAGBs and concentrated below misorientation angle of 3°, while the GND density distribution is primarily falling within the range of 0–1.5 × 10^{14}/m^2.

IGC tests were performed to evaluate the effect of processing on the corrosion resistance. Fig. 11 presents the results of the IGC tests, including the observed metallographic images of specimens' cross-sections after 24 h immersion and the calculated corrosion rates across various initial states. Figs. 11a and b demonstrate the cross-sectional images after 24 h immersion of specimens of the as-received and PA with subsequent 6 h creep-ageing respectively. Different corrosion morphologies can be observed after 24 h immersion in these two different states. When evaluating the IGC penetration depth of the as-received (Fig. 11a) and PA & CA (Fig. 11b), the latter is more prone to activating corrosion paths to the former, resulting in a larger corrosion depth at the end of the test. In addition, a larger area of intragranular corrosion can be observed in the PA & CA specimen compared to the as-received. The differences in corrosion morphologies indicate that the material's corrosion resistance varies with the applied treatment.

To quantitively compare the effects of various treatments on the corrosion resistance of the material, the corrosion rates in the IGC tests are calculated using the widely adopted equation as [34].

$$CR = \frac{w_0 - w_1}{At\rho} \tag{1}$$

where w_0 and w_1 represent the specimen weight before and after the IGC test, A is the exposed specimen surface area in the IGC solution, and t is the total immersion time i.e. 24 h in the current study, and ρ is the material density. According to this definition, the corrosion rate CR has a unit of mm/h, and a higher value of CR indicates a lower corrosion resistance of the material in practical service. Fig. 11c demonstrates the corrosion rate results. Across all the treatment conditions, the PA & CA condition exhibits the highest corrosion rate at 0.03 mm/h, while the as-received has the lowest rate at 0.019 mm/h. The corrosion rate for the PA & CA condition is 1.57 times higher than that of the as-received. For the remaining conditions including CA, TCA & CA, and CCA & CA, similar corrosion rates are identified with a maximum difference of 0.002 mm/h between TCA & CA and CCA & CA.

4. Discussion

4.1. Microstructural evolution across various pre-treatments

This study introduced three different pre-treatments, i.e. pre-ageing, tensile creep-ageing, and compressive creep-ageing, all conducted at the same temperature of 174 °C for 1 h. The key difference among the three treatments lies in the applied stress that PA was stress-free, while TCA and CCA were performed under 120 MPa along the tensile and compressive directions respectively. In addition, when compared to the as-received material, the ageing (PA) and creep-ageing (TCA, CCA) pre-treatments induced the variations in microstructure that influenced the microstructural evolutions during the subsequent creep-ageing process. Therefore, it is crucial to discuss the effects of ageing/stress ageing adopted in the pre-treatment stage on the observed differences in microstructural evolution among various pre-treated conditions, as well as in comparison to the as-received condition.

4.1.1. Precipitates evolution

As shown in Fig. 8, the size increase for both the GP zone and η' precipitate has a unified trend across all treatment conditions, with the extent of increase much more significant for η' precipitate than GP zone. The competition in precipitation evolution among the major

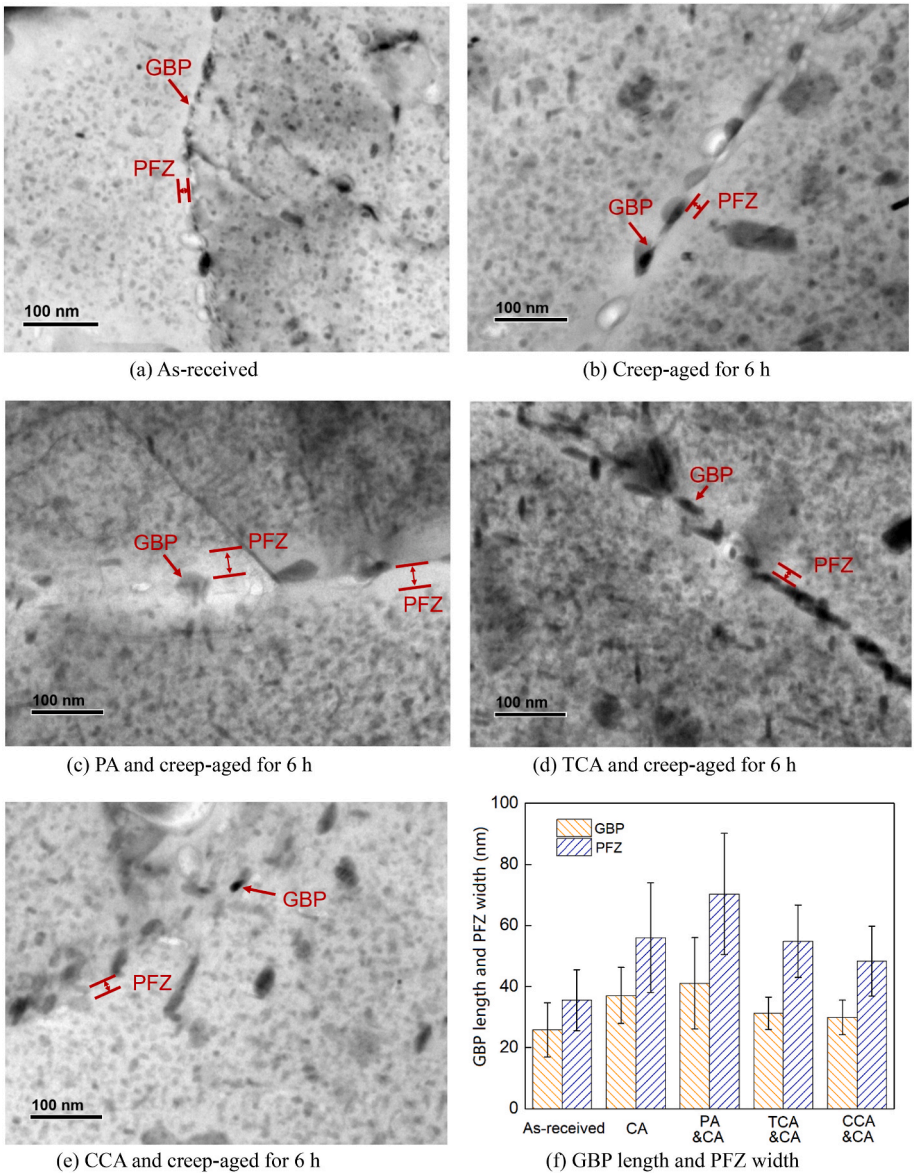

Fig. 9. TEM images and statistical results of grain boundaries from specimens in the as-received state, creep-aged for 6 h, and subjected to different pre-treatments with subsequent 6 h creep-ageing. The notations "GBP" and "PFZ" respectively represent the grain boundary precipitate and precipitate free zone.

strengthening phases has been observed in both 2xxx and 7xxx aluminium alloys [35,36]. The attraction of the same limited solute atoms in the alloy matrix by various precipitates can promote the size increase of one phase at the expense of others [36]. Zn and Mg are the dominant solute atoms composing both the GP zone and η' precipitate, supplied by the $MgZn_2$ precursor clusters in the alloy matrix and transported through diffusion [31,37]. In addition, the activation energy required for Zn and Mg solute atoms migration to η' precipitate is approximately twice that required for GP zone [37]. With the supplement of excessive kinetic energy induced by the ageing and creep-ageing treatment, the higher energy barrier for η' precipitate to capture Zn and Mg solute atoms can be satisfied. This promotes the further evolution of the η' precipitate beyond the GP zone, driven by the system's tendency to reduce total Gibbs free energy and achieve improved stability, since η' precipitate possesses a lower free energy than GP zone [38,39]. As a result, the number ratios of η' precipitate all increase with the creep-ageing treatment as shown in Fig. 8c. As more Zn and Mg solute atoms are consumed during the evolution of η' precipitate causing the restraint of GP zone evolvement, the size and number ratio of η' precipitate become greater than that of GP zone during creep-ageing process across various conditions as demonstrated in Fig. 8.

When comparing the size increase of η' precipitate subjected to various pre-treatments followed by 6 h creep-ageing, the evolution with TCA and CCA conditions demonstrates the largest increases with a size increase of 13.1 and 12 nm respectively, as shown in Fig. 8b. In contrast, the conditions of as-received & CA and PA & CA exhibit lower precipitate size increases, with the former exhibiting the least increasing of 6.5 nm, less than half of the increase of TCA & CA condition. In addition, the number ratios of η' precipitate in the TCA & CA and CCA & CA states are higher than the PA & CA and CA states as shown in Fig. 8c. The variation in evolution of η' precipitate at the end of creep-ageing across different conditions can be attributed to the effect of dislocations introduced prior and during creep-ageing. Dislocation cores can work as channels for transportation of solute atoms at a rate magnitudes higher than those through diffusion in the alloy matrix [40,41]. Therefore, in this study, with the pre-introduced extra dislocations in the pre-treatment stage of TCA and CCA, along with the higher deformation induced dislocations in the subsequent creep-ageing stage, the evolution of η' precipitates in these two conditions surpassed that observed in the other treatment

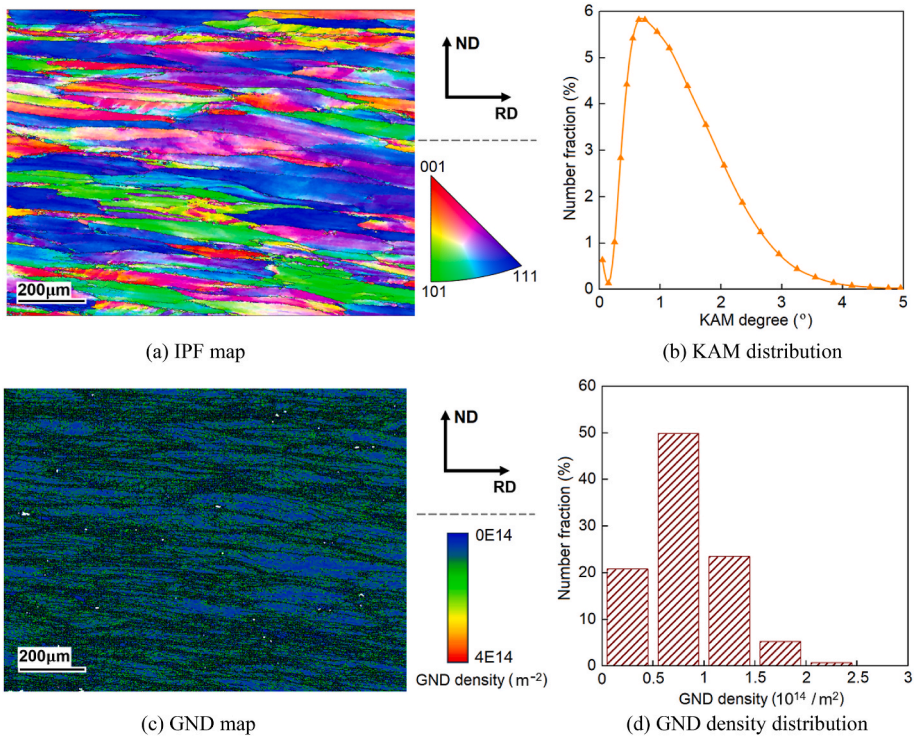

Fig. 10. EBSD analysis results for the material in the as-received state, including (a) the IPF figure, (b) KAM distribution, (c) GND map, and (d) GND density distribution. "RD" and "ND" denote the specimen orientation of rolling and normal directions. The black lines in (c) exhibit the LAGBs. The columns in (d) stands for the fraction of the GND density in the range.

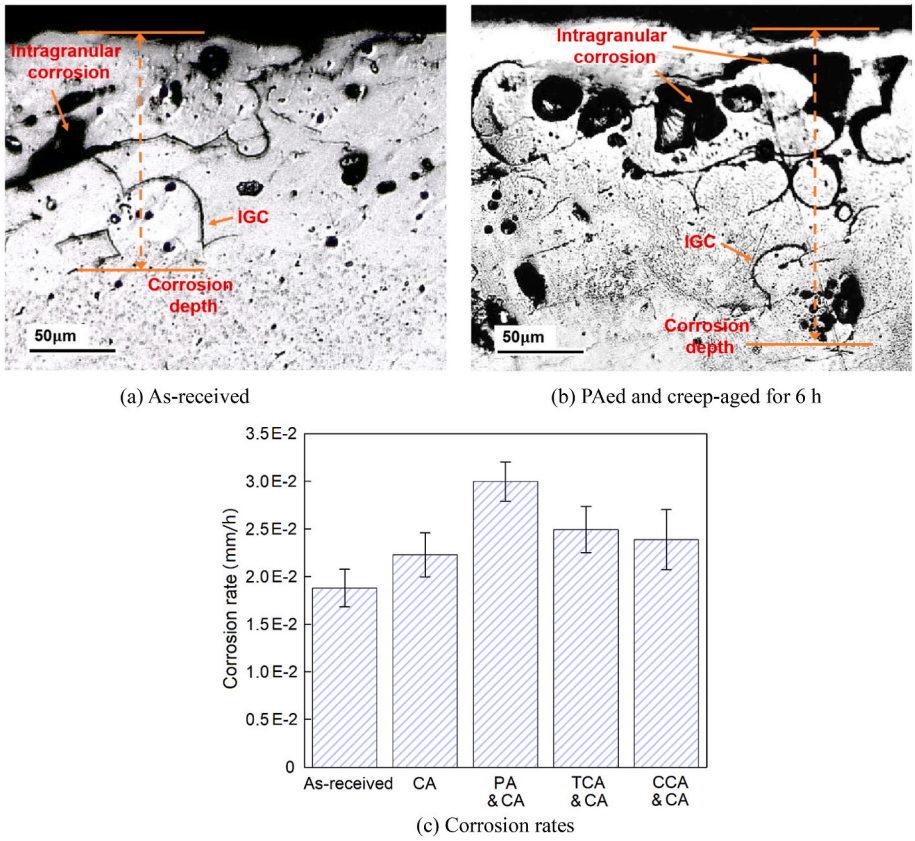

Fig. 11. Cross-sectional metallographic images of specimens after immersion in IGC solution for 24 h and the calculated corrosion rates across various treatment states. The notations in (c) represent immersion in IGC solution for 24 h in the following states including as-received state (As-received), after creep-ageing for 6 h (CA), PA and CA for 6 h (PA & CA), TCA and CA for 6 h (TCA & CA), and CCA and CA for 6 h (CCA & CA).

conditions. Fig. 12 demonstrates the evolution of observed precipitates in AA7475 TAF temper with creep-ageing across various states.

4.1.2. PFZs and GBPs evolution

The precipitate free zones observed in Fig. 9 demonstrate a consistent morphology across various conditions where grain boundary precipitates are nucleated and grow along the grain boundary, with PFZs forming on each side of the boundary. The grain boundary serves as a sink for vacancies providing heterogeneously nucleation sites for precipitates, which leads to solute depletion and formation of PFZs along the boundary [42,43]. In Al-Zn-Mg-Cu alloys, the GBPs are predominantly composed of coarsened η precipitate and E phase particles $Al_{18}Mg_3Cr_2$ [44,45], possessing a larger average size than precipitates within the grain as demonstrated in Fig. 9. On the other hand, also shown in Fig. 9, variations in the width of the PFZ, as well as the distribution and size of the GBPs can be identified across different pre-treatments.

Previous investigation observed that when the material is subjected to low deformation (strain less than 10 %), the corresponding induced dislocations are prone to accumulate within PFZs as softer regions compared to the grain interior [46]. In addition, LAGBs act as barriers that cause dislocations propagated within the grain to impinge on the boundary networks during deformation, driven by the geometric and structural stabilisation effects of LAGBs [47]. For the TAF temper AA7475 adopted in this study, as demonstrated in Fig. 10, the grain boundaries of the material are predominantly composed of LAGBs. Additionally, the GNDs mostly surround the grain boundaries. Therefore, with the existing dislocations and additional ones accumulated along the grain boundary during creep-ageing that provides more solute diffusion paths and enhances diffusion rates, a general increasing trend in the GBPs can be observed when compared to the as-received state. Variations in grain boundary evolutions can also be identified under different pre-treatment conditions as shown in Fig. 9f. In the PA & CA specimen, the GPB size is larger than the other three conditions. This difference can be attributed to the dissolution of smaller precipitates near the grain boundary as well as GBPs during the pre-ageing treatment, which enriches the limited solute atoms such as Mg, Zn, and Cu in the grain boundary area, thus further facilitating the evolution of the existing GBPs driven by the sink effect of the grain boundary in the subsequent creep-ageing [45,48]. In addition, with the acceleration of solution depletion with increasing GBPs, a wider PFZ resulted from creep-ageing of the PA specimen. In specimens undergone TCA or CCA pre-treatments, more densely distributed GBPs can be observed as demonstrated in Fig. 9d and e. The additional dislocations introduced by TCA and CCA treatments increase the heterogenous nucleation sites, thereby enhancing the number of GBPs while restraining their size due to more intense competition for the limited solute atoms within the grain boundary area. Moreover, the increased dislocations can provide new sites for precipitates nucleation in the PFZ area, leading to a narrower PFZ in the TCA/CCA & CA specimens. The schematic of microstructural evolutions within grain boundary areas of TAF temper AA7475 across various treatments is further illustrated in Fig. 13.

4.2. Material behaviour across various pre-treatments

A reduction in material strength to varying extents after pre-treatment, as well as subsequent creep-ageing compared to the as-received state is demonstrated in Fig. 6. The strength variation in the ageing and creep-ageing processes is closely related to the evolutions of the precipitate and dislocation interactions throughout the processes [18,35]. When dislocations encounter precipitates as obstacles during glide and climb in deformation, the interaction mechanisms include dislocations cutting through smaller precipitates (i.e. shearing) or bypassing coarsened ones. The evolution of precipitate size in these interactions leads to variations in the critical resolved shear stress (CRSS) and affects the material's strength as described by the following equations [18].

$$\begin{cases} \sigma_A = A\bar{r}^{m_a} \\ \sigma_B = B/\bar{r}^{m_b} \end{cases} \tag{2}$$

where σ_A and σ_B are respectively the precipitation hardening contributed by dislocation shearing through and looping over precipitates, $\bar{r}$ is the precipitate size, and A, B, m_a and m_b are material constants. It should be note that as manifested by the equation, an increase in precipitate size can enhance the resistance to shearing but decrease resistance in looping over. Therefore, the reduction in strength and the observed increase in precipitates size of TAF temper AA7475 with further ageing and creep-ageing indicate that precipitate coarsening is the dominant factor. The coarsening of precipitates transforms the strengthening mechanism from shearing to bypassing during deformation, leading to a decrease in material strength.

On the other hand, a contrast is observed between the minor divergences in strength and the varying degrees of precipitates coarsening among the pre-treated specimens (PA, TCA, and CCA), as shown in Figs. 6 and 8. It should be noted that apart from precipitate hardening, material strength can also be influenced by other factors such as dislocation density. The presence of PFZs can be detrimental to the material strength due to the lack of finely distributed strengthening precipitates

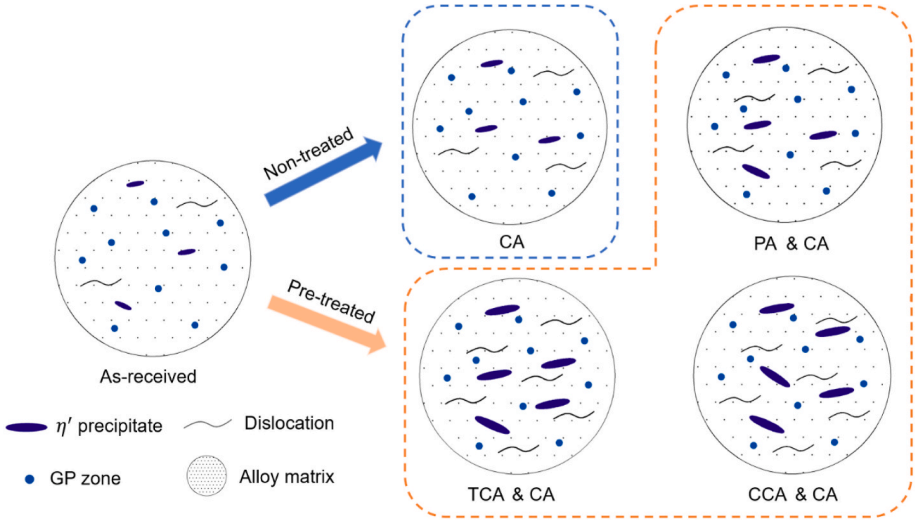

Fig. 12. Schematic of microstructure evolutions in TAF temper AA7475 creep-aged across various treatments.

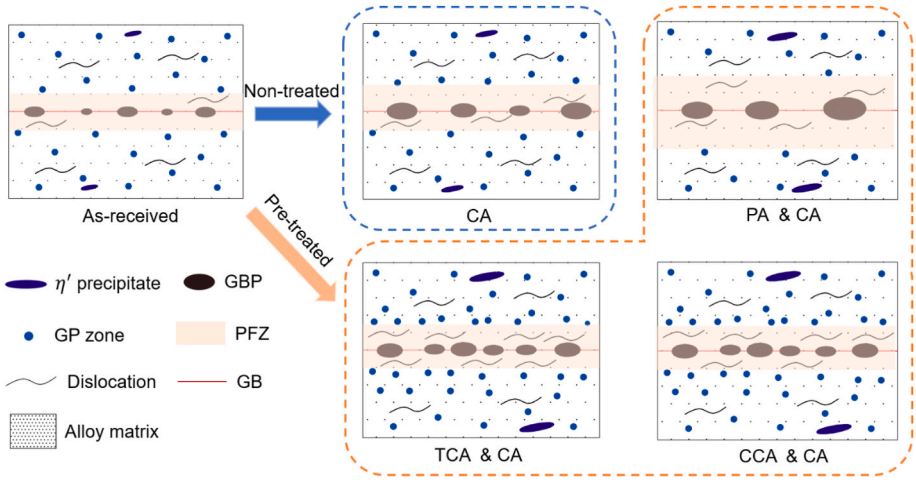

Fig. 13. Schematic of microstructural evolutions within grain boundary areas of TAF temper AA7475 across various treatments.

within the areas [49,50]. Furthermore, the accumulation of dislocations as pile-ups can act as obstacles during deformation, which can increase the contribution of dislocation hardening to material strength. Therefore, the reduced width of PFZs, as well as the increased dislocations introduced in the TCA and CCA pre-treated specimens, can be beneficial to the material strength. This compensates for the loss in strength caused by more coarsened precipitates, maintaining the strength at a level comparable the PA specimen.

The creep deformation behaviour of AA7475 in TAF temper demonstrates significant differences after the 1 h pre-treatments, with a deformation ratio ranging from 1.4 to 1.6 compared to the as-received state as shown in Fig. 4. Creep deformation behaviour is known to be significantly influenced by dislocations and their interactions with the precipitates within the alloy [51,52]. For the pre-treated specimens, the coarsened precipitates provide less resistance to dislocation movements through bypassing, thereby promoting creep deformation under the same stress and temperature compared to the as-received specimen. Furthermore, the pre-deformation introduced additional moveable dislocations can effectively decrease the threshold stress required to initiate creep deformation [14,53]. As a result, more dislocation slips and climbs can be activated, leading to an increased creep deformation rate [54,55]. Therefore, in the TCA and CCA pre-treated specimens, the extra moveable dislocations introduced during the pre-treatment stage promote creep deformation in the subsequent creep-ageing stage. It should also be noted that the PFZs can also exerts effects on creep deformation as softer regions lacking finely distributed strengthening precipitates, with a wider PFZ leading to a lower creep resistance [50].

4.3. Corrosion resistance across various treatments

As shown in Fig. 11, the corrosion resistance of AA7475 generally decreased after subsequent creep-ageing tests across various states. For Al-Zn-Mg-Cu alloys, anodic dissolution is widely recognised as the dominant corrosion mechanism, which is an electromechanical behaviour strongly influenced by the microstructures within the grain boundary regions [4,9]. The differences in corrosion potentials in the alloy matrix (−0.68 V), PFZs (−0.57 V), and GBPs (−0.87 V) of Al-Zn-Mg-Cu alloys constitute an electrochemical system with multiple couples among these components [8,46]. In this system, GBPs and the alloy matrix act as anodes when coupled with PFZs, making GBPs and the alloy matrix more susceptible to be corroded during intergranular and intragranular corrosions [30,46]. It should be noted that the electrochemical coupling between PFZs and GBPs exhibits the largest corrosion potential difference, indicating a dominant susceptibility to corrosion within the system. After creep-ageing of TAF temper AA7475, the evolutions of PFZs and GBPs can reduce corrosion resistance and accelerate IGC in the creep-aged specimens across various states as shown in Fig. 11. Specifically, for the PA pre-treated specimen, the lowest corrosion resistance is induced by the largest average PFZ width and GBP size when compared to the others.

In addition, among the corrosion resistance of the creep-aged specimens of as-received, and pre-treated with TCA and CCA, the latter two demonstrate a lower resistance trend despite having similar or even smaller PFZ width and GBP size when compared to the directly creep-aged condition, as illustrated in Figs. 9f and 11c. This discrepancy can be attributed to the distribution of GPBs when acting as the anode in IGC process to influence the progression of corrosion. When GBPs are more continuously distributed along the grain boundary, the GBPs create a more active corrosion path for galvanic reaction which promotes the susceptibility to IGC [7,30]. As shown in Fig. 9c and d, the TCA and CCA pre-treatments create a more continuous distribution of GBPs during the subsequent creep-ageing, and thus provide more corrosion paths in the IGC process. On the other hand, a larger spacing of GBPs in the directly creep-aged specimen prevents further reactions along the grain boundaries and leads to higher corrosion resistance, despite having similar PFZ width and GBP size compare to the TCA and CCA pre-treated and creep-aged conditions.

4.4. Treatment strategies for multi-step aged AA7475

In this study, the as-received material AA7475 had undergone the treatment procedure including SHT, followed by 2 %–3 % pre-deformation, and a multi-step ageing treatment to achieve the TAF temper, which provides material property comparable to T74 temper with significantly reduced processing time [26]. On the other hand, due to the increased strength of the material after the treatment, the creep deformation accumulated after 6 h of creep ageing was only 0.08 %, indicating a low production efficiency at this deformation rate. In this study, two types of pre-treatments, stress-free ageing and stressed ageing, were conducted to investigate alternative routines for improving CAF efficiency while maintaining acceptable material strength and corrosion resistance. By comparing the results across all conditions (with and without pre-treatments), multiple routines with different priority criteria can be identified. For the PA condition, the creep deformation increased by nearly 40 % compared to the as-received condition. In addition, the strength reduction was lower than that observed in the TCA and CCA conditions. Therefore, the PA treatment can be considered suitable when the service condition of the fabricated component is strength-critical. On the other hand, for the TCA and CCA pre-treatments, greater creep deformation promotion and improved corrosion resistance were achieved compared to the PA treatment. However, the strength reductions were also higher than observed in the

PA condition. This suggests that in situations where corrosion resistance is critical, stressed-ageing treatments can be adopted as the optimised options. It should also be noted that although the material strength and corrosion resistance of the as-received material demonstrated superior performances compared to the pre-treated conditions after creep-ageing, the much lower deformation rate indicates that a significantly longer creep-ageing time is required during CAF fabrication. This extended ageing time can lead to a substantial reduction in strength and corrosion resistance due to precipitate coarsening and PFZ widening, making the pre-treatment routines superior options by offering increased fabrication efficiency with acceptable reductions in material strength and corrosion resistance during CAF.

5. Conclusions

In this study, experimental investigations into the creep deformation behaviour and the evolutions of material strength and corrosion resistance during creep-ageing have been conducted for a multi-step aged AA7475 subjected to various pre-treatments. The corresponding microstructural evolution within the alloy matrix and the grain boundary areas have been investigated, based on which the correlation between the microstructural evolution and material behaviour have been analysed. The following conclusions can be drawn:

1. Pre-treatments including stress-free ageing and stressed ageing can promote creep deformation of multi-step aged AA7475 in the temper for age forming (TAF) during subsequent creep-ageing process compared to the as-received state, with a maximum deformation promotion of 1.94 times for the tensile creep aged (TCA) treatment when creep-aged at 174 °C under 135 MPa for 6 h.
2. For AA7475 in the TAF temper, both material strength and corrosion resistance decrease under all conditions after creep-ageing. When compared to the as-received material, the TCA pre-treated specimens exhibit the largest reduction in material strength, while those with pre-aged (PA) initial state have the most decrease in corrosion resistance after creep-ageing.
3. The evolution of GP zones and η' precipitates in TAF temper AA7475 during creep-ageing is dominated by precipitate coarsening for both the as-received and pre-treated specimens. In the pre-treated specimens, the coarsening of η' precipitates is further accelerated, resulting in a larger increase in precipitate size and corresponding reduction in material strength after creep-ageing.
4. Different pre-treatments induce the increases in GBP size and PFZ width as well as the varying distribution of precipitates in the grain boundary area during creep-ageing to various extents. This difference in grain boundary evolution can be attributed to different dislocation densities introduced in the grain boundary area by different pre-treatments, leading to varying corrosion resistance.

CRediT authorship contribution statement

Xi Wang: Writing – original draft, Methodology, Investigation. **Zhusheng Shi:** Writing – review & editing, Supervision, Conceptualization. **Jianguo Lin:** Writing – review & editing.

Declaration of competing interest

The authors declare that they have no known competing financial interests or personal relationships that could have appeared to influence the work reported in this paper.

Appendix A. Test results for the strength evolution under various conditions

To further validate the observed strength evolution trend of the material creep-aged under various conditions, repeated tests were conducted for the as-received condition, pre-aged (PA) treatment, creep-aged (CA) for 6 h, and tensile creep-aged (TCA) with CA for 6 h, with the results shown in Table A1. As can be observed, the results demonstrated acceptable consistency, with a maximum divergence of 5 MPa (1.2 %) for the CA condition.

Table A1
Test results for the strength evolution under various conditions

	As-received	PA	CA	TCA & CA
Tensile test 1 (MPa)	455	450	424	410
Tensile test 2 (MPa)	458	451	419	406
Average (MPa)	456.5	450.5	421.5	408

Data availability

Data will be made available on request.

References

[1] T. Dursun, C. Soutis, Recent developments in advanced aircraft aluminium alloys, Mater. Des. 56 (2014) 862–871.
[2] F. Min, K. Gao, W. Wei, X. Wu, S. Wen, H. Huang, et al., Ballistic resistance of 7XXX laminate aluminum alloy plates and base alloys subjected to different projectiles, Int. J. Impact Eng. 191 (2024) 104998.
[3] D. Zhang, H. Jiang, Z. Cui, D. Yan, Y. Song, L. Rong, Synchronous improvement of mechanical properties and stress corrosion resistance by stress-aging coupled with natural aging pre-treatment in an al-zn-mg alloy with high recrystallization fraction, J. Mater. Sci. Technol. 121 (2022) 40–51.
[4] B. He, X. Wu, L. Cao, S. Tang, Y. Yang, Y. Zou, Revealing the mechanisms of exfoliation corrosion and stress corrosion cracking for an al-zn-mg-cu alloy after continuous retrogression and re-ageing treatment, Corros. Sci. 240 (2024) 112474.
[5] A. Azarniya, A. Taheri, K. Taheri, Recent advances in ageing of 7xxx series aluminum alloys: a physical metallurgy perspective, J. Alloys Compd. 781 (2019) 945–983.
[6] Y. Liu, M. Wang, X. Liu, C. Yan, Z. Li, B. Okonkwo, et al., The effect of combination of pre-ageing and regression heat treatment on the natural aging behavior in al–zn–mg–cu alloys correlated with precipitate dissolving ratio, J. Mater. Res. Technol. 31 (2024) 2972–2984.
[7] W. Yang, Y. Zhang, H. Yang, L. Zhang, S. Zheng, M. Li, Effect of non-isothermal retrogression and re-aging treatment on microstructure evolution and mechanical properties of al–zn–mg–cu alloy, J. Mater. Res. Technol. 31 (2024) 1728–1743.
[8] W. Yang, S. Ji, Q. Zhang, M. Wang, Investigation of mechanical and corrosion properties of an al–zn–mg–cu alloy under various ageing conditions and interface analysis of η′ precipitate, Mater. Des. 85 (2015) 752–761.
[9] B. He, L. Cao, X. Wu, S. Tang, X. Lin, Y. Zou, Effect of continuous retrogression and re-ageing treatment on mechanical properties, corrosion behavior and microstructure of an al-zn-mg-cu alloy, J. Alloys Compd. 970 (2024) 172592.
[10] C. Lei, H. Yang, H. Li, N. Shi, L. Zhan, Dependences of microstructures and properties on initial tempers of creep aged 7050 aluminum alloy, J. Mater. Process. Technol. 239 (2017) 125–132.
[11] Y. Huang, Y. Liu, Z. Xiao, Y. Huang, A trade-off between mechanical strength and electrical conductivity of al–zn–mg–cu alloy via Ag alloying and retrogression re-aging heat treatment, Mater. Sci. Eng. 880 (2023) 145230.
[12] L. Zhan, J. Lin, T.A. Dean, A review of the development of creep age forming: experimentation, modelling and applications, Int. J. Mach. Tool Manufact. 51 (2011) 1–17.

[13] F. Ribeiro, E. Marinho, D. Inforzato, P. Costa, G. Batalha, Creep age forming: a short review of fundaments and applications, J. Achiev. Mater. Manuf. Eng. 43 (2010) 353–361.
[14] X. Wang, Q. Rong, Z. Shi, J. Lin, An efficient closed-form solution for springback prediction and compensation in elastic–plastic creep age forming, Int. J. Adv. Des. Manuf. Technol. 125 (2023) 1115–1133.
[15] Q. Rong, Z. Shi, Y. Li, J. Lin, Constitutive modelling and its application to stress-relaxation age forming of AA6082 with elastic and plastic loadings, J. Mater. Process. Technol. 295 (2021) 117168.
[16] F. Brandão, S. Delijaicov, R. Bortolussi, CAF—A simplified approach to calculate springback in Al 7050 alloys, Int. J. Adv. Des. Manuf. Technol. 91 (2017) 3273–3284.
[17] F. Lyu, Y. Li, X. Huang, Z. Shi, Y. Zeng, J. Lin, An investigation of creep age forming of AA7B04 stiffened plates: experiment and FE modelling, J. Manuf. Process. 37 (2019) 232–241.
[18] X. Wang, Q. Rong, Z. Shi, J. Lin, Improved creep behaviour for a high strength Al-Li alloy in creep age forming: experimental studies and constitutive modelling, Int. J. Plast. 159 (2022) 103447.
[19] J. Zhang, Z. Li, F. Xu, C. Huang, Regulating effect of pre-stretching degree on the creep aging process of al-cu-li alloy, Mater. Sci. Eng. 763 (2019) 138157.
[20] Y. Yang, L. Zhan, R. Shen, X. Yin, X. Li, W. Li, et al., Effect of pre-deformation on creep age forming of 2219 aluminum alloy: experimental and constitutive modelling, Mater. Sci. Eng. 683 (2017) 227–235.
[21] J. Zheng, R. Pan, C. Li, W. Zhang, J. Lin, C. Davies, Experimental investigation of multi-step stress-relaxation-ageing of 7050 aluminium alloy for different pre-strained conditions, Mater. Sci. Eng. 710 (2018) 111–120.
[22] L. Xu, C. Tong, L. Zhan, Y. Xu, C. Liu, M. Huang, et al., Improved creep forming efficiency and retained performance via a novel two-stage creep aging process of al–zn–mg–cu alloys, Mater. Sci. Eng. 851 (2022) 143581.
[23] L. Zhang, T. Bian, H. Li, X. Yang, C. Lei, Stress relaxation aging of 7050 aluminum alloy under elastic and plastic loadings: a perspective from the geometrically necessary dislocations, J. Alloys Compd. 1010 (2025) 177066.
[24] Y. Ren, T. Wan, Y. Xu, K. Zhang, M. Zhang, J. Li, Effects of stress aging treatment on the microstructure, mechanical properties and electrochemical corrosion behavior of al-zn-mg-cu alloy, J. Alloys Compd. 997 (2024) 174686.
[25] Y. Lin, J. Zhang, G. Liu, Y. Liang, Effects of pre-treatments on aging precipitates and corrosion resistance of a creep-aged al–zn–mg–cu alloy, Mater. Des. 83 (2015) 866–875.
[26] J. Costa, N. Moura, D. Wade, Evaluation of a 7050-TAF aluminum alloy submitted to creep age forming, Mater. Res. 17 (2014).
[27] K. Wang, A. Naumov, M. Gushchina, F. Isupov, Ai Alkhalaf, O. Panchenko, The effect of impulses on precipitation behavior in 7075-T6 aluminum alloy joint by impulse friction stir welding, Int. J. Adv. Des. Manuf. Technol. 128 (2023) 373–389.
[28] L. Xu, L. Zhan, Y. Xu, C. Liu, M. Huang, Thermomechanical pretreatment of al-zn-mg-cu alloy to improve formability and performance during creep-age forming, J. Mater. Process. Technol. 293 (2021) 117089.
[29] K. Wen, Y. Fan, G. Wang, L. Jin, X. Li, Z. Li, et al., Aging behavior and fatigue crack propagation of high Zn-containing al-zn-mg-cu alloys with zinc variation, Prog. Nat. Sci. Mater. Int. 27 (2017) 217–227.
[30] H. Zhong, S. Li, J. Wu, H. Deng, J. Chen, N. Yan, et al., Effects of retrogression and re-aging treatment on precipitation behavior, mechanical and corrosion properties of a Zr+Er modified al-zn-mg-cu alloy, Mater. Char. 183 (2022) 111617.
[31] S. Liu, H. Hou, W. Shao, J. Yang, Z. Wang, Q. Yang, et al., Revisiting the precipitation mechanisms of Guinier-Preston zones, η′, and η precipitates in al-zn-mg alloys, Acta Mater. 268 (2024) 119789.
[32] H. Zhang, H. Li, W. Peng, Z. Jiang, K. Ma, L. Lin, et al., Effect of applied stress level on anisotropy in creep-aging behavior of al–cu–li alloy, J. Mater. Res. Technol. 27 (2023) 4390–4402.
[33] J. Zhang, J. Fan, L. Chen, Y. Li, Compressive creep aging behavior and microstructure evolution in extruded al-mg-si alloy under different temperature and stress levels, Mater. Today Commun. 33 (2022) 104722.
[34] F. Malaret, Exact calculation of corrosion rates by the weight-loss method, Exp. Results 3 (2022) 13.
[35] X. Wang, Q. Rong, Z. Shi, Y. Li, J. Cao, B. Chen, et al., Investigation of stress effect on creep, precipitation and dislocation evolution of Al–Li alloy during creep age forming, Mater. Sci. Eng. 836 (2022) 142723.
[36] L. Liu, Q. Shao, T. Fan, D. Yuan, J. Chen, The precipitation competition of η-series precipitates and δ' precipitates in Li-containing al-zn-mg-cu alloys, Comput. Mater. Sci. 198 (2021) 110707.
[37] A. Khalfallah, A. Raho, S. Amzert, A. Djemli, Precipitation kinetics of GP zones, metastable η′ phase and equilibrium η phase in Al−5.46wt.%Zn−1.67wt.%Mg alloy, Trans. Nonferrous Metals Soc. China 29 (2019) 233–241.
[38] C. Wu, K. Ma, D. Zhang, J. Wu, S. Xiong, G. Luo, et al., Precipitation phenomena in al-zn-mg alloy matrix composites reinforced with B4C particles, Sci. Rep. 7 (2017) 9589.
[39] G. Sha, A. Cerezo, Early-stage precipitation in al–zn–mg–cu alloy (7050), Acta Mater. 52 (2004) 4503–4516.
[40] F. Liu, A. Cocks, E. Tarleton, A new method to model dislocation self-climb dominated by core diffusion, J. Mech. Phys. Solid. 135 (2020) 103783.
[41] T. Nakajima, M. Takeda, T. Endo, Accelerated coarsening of precipitates in crept Al–Cu alloys, Mater. Sci. Eng. 387–389 (2004) 670–673.
[42] Y. Chen, S. Pan, S. Tang, W. Liu, C. Tang, F. Xu, Formation mechanisms and evolution of precipitate-free zones at grain boundaries in an al–cu–mg–mn alloy during homogenisation, J. Mater. Sci. 51 (2016) 7780–7792.
[43] B. Cai, B. Adams, T. Nelson, Relation between precipitate-free zone width and grain boundary type in 7075-T7 Al alloy, Acta Mater. 55 (2007) 1543–1553.
[44] P. Cao, G. Xie, C. Li, D. Zhu, Feng Di, B. Xiao, et al., Investigation of the quenching sensitivity of the mechanical and corrosion properties of 7475 aluminum alloy, Metals 13 (2023) 1656.
[45] M. Afifi, Y.C. Wang, P. Pereira, Y.W. Wang, S. Li, Y. Huang, et al., Characterization of precipitates in an al-zn-mg alloy processed by ECAP and subsequent annealing, Mater. Sci. Eng. 712 (2018) 146–156.
[46] M. Wu, D. Xiao, S. Yuan, Y. Huang, Z. Li, X. Yin, et al., Healing the high-temperature-retrogression-caused wide precipitation-free zones in al-zn-mg-cu alloy via strain-aging induced precipitates, Mater. Sci. Eng. 917 (2024) 147398.
[47] S. Kondo, T. Mitsuma, N. Shibata, Y. Ikuhara, Direct observation of individual dislocation interaction processes with grain boundaries, Sci. Adv. 2 (2016) e1501926.
[48] Y. Zou, X. Wu, S. Tang, Y. Wang, K. Zhao, L. Cao, The effect of pre-ageing/stretching on the ageing-hardening behavior of al–zn–mg–cu alloys correlated with Zn/Mg ratio, Mater. Sci. Eng. 830 (2022) 142331.
[49] T. Krol, D. Baither, E. Nembach, Quantification of the detrimental effects of precipitate free zones on the yield strength of a superalloy, Scr. Mater. 48 (2003) 1189–1194.
[50] X. Chen, X. Zheng, M. Pan, Y. Liu, Y. Kong, A. Hartmaier, et al., Effect of precipitation-free Zone on fatigue properties in Al-7.02Mg-1.98Zn alloys: crystal plasticity finite element analysis, Materials 17 (2024) 5623.
[51] Q. Rong, Y. Li, Z. Shi, L. Meng, X. Sun, J. Lin, Experimental investigations of stress-relaxation ageing behaviour of AA6082, Mater. Sci. Eng. 750 (2019) 108–116.
[52] X. Wang, Z. Shi, C. Sun, J. Lin, Investigation of anisotropy evolution of an aluminium-lithium alloy with increasing pre-deformation in creep age forming, Mater. Char. 206 (2023) 113378.
[53] C. Liu, J. Yang, P. Ma, Z. Ma, L. Zhan, K. Chen, et al., Large creep formability and strength–ductility synergy enabled by engineering dislocations in aluminum alloys, Int. J. Plast. 134 (2020) 102774.
[54] B. Zhao, P. Huang, L. Zhang, S. Li, Z. Zhang, Q. Yu, Temperature effect on stacking fault energy and deformation mechanisms in titanium and titanium-aluminium alloy, Sci. Rep. 10 (2020) 3086.
[55] F. Liu, A. Cocks, E. Tarleton, Dislocation dynamics modelling of the creep behaviour of particle-strengthened materials, Proc. R. Soc. A 477 (2021) 20210083.